WING SHAPE CONTROL ON THE D150 MODEL WITH ASPECT RATIO TRADEOFFS FOR FUEL EFFICIENCY IMPROVEMENT

Fanglin Yu[1], Carlos Sebastia Saez[1], Mirko Hornung[1], Milán Barczi[2], Béla Takarics[2], Yasser M. Meddaikar[3]

[1] Technical University of Munich
Boltzmannstrasse 15, 85748 Garching, Germany
fanglin.yu@tum.de
carlos.sebastia@tum.de
mirko.hornung@tum.de

[2]HUN-REN Institute for Computer Science and Control (SZTAKI)
H-1111 Budapest, Kende u. 13-17.
barczimilan@sztaki.hu
takarics@sztaki.hu

[3]DLR - Institute of Aeroelasticity,
Bunsenstrasse 10, 37073 Goettingen, Germany
Muhammad.Meddaikar@dlr.de

Keywords: Wing shape control, drag reduction, aeroelasticity, high aspect ratio

Abstract: This study investigates the implementation of wing shape control using control surfaces to reduce drag and enhance aerodynamic performance. It evaluates several aerodynamic modeling methods with focus on drag—namely, the Vortex Lattice Method, Doublet Lattice Method, and 3D Panel Method. Drag optimization was conducted on the D150 aircraft model, representative of short- to medium-range configurations, to determine the optimal control surface scheduling. The analysis included wings with aspect ratios of 9.7 and 11.2, exploring three distinct control surface layouts to ascertain the most effective control surface layout. The findings indicate that a drag reduction ranging from 1.5% to 2.5% is achievable on the wing with a nominal aspect ratio using 10 multifunctional control surfaces, underscoring the potential of wing shape control in improving aircraft efficiency.

1 INTRODUCTION

Reducing the carbon footprint is an urgent concern for the aviation industry. Given that alternative fuels are not expected to be viable in the near future, enhancing aircraft performance has become increasingly critical. In addition to improving engine efficiency and reducing structural weights, enhancing aerodynamic efficiency is an effective approach to improve aircraft performance. Using control surfaces to achieve optimal lift distribution and reduce induced drag is a promising strategy for boosting aerodynamic efficiency.

Aircraft wings are typically designed to be optimal for a specific flight condition and a mass case. However, throughout an aircraft's mission, the fuel stored in the wings is gradually consumed, leading to changes in mass, which in turn can alter the wing loading, wing shape, and lift distribution due to aeroelastic effects. Moreover, operational considerations may require the aircraft to operate under flight conditions that differ from the design cruise condition, resulting in

suboptimal aerodynamic performance. In such scenarios, wing shape control, via trailing edge control surfaces, plays a crucial role in restoring optimal lift distribution and thereby improving overall aerodynamic performance.

Several researchers have explored the technology of using control surfaces to control wing shape for drag reduction. Reist [1] demonstrated that employing existing control surfaces as variable camber on a business jet can decrease drag by approximately 1-5% across various cruise conditions. Lebofsky [2] investigated the Variable Camber Continuous Trailing Edge (VCCTE) flap system on NASA Generic Transport Model, utilizing active control of wing aeroelastic deflections to enhance aerodynamic efficiency by reducing cruise drag. Additionally, Nguyen [3] demonstrated a 3.37% drag reduction for Mach 0.85 in a real-time drag optimization study using the 13.5 aspect ratio (AR) Common Research Model, which was equipped with a distributed mini-plain flap system.

The FLIPASED (Flight Phase Adaptive Aero-Servo-Elastic Aircraft Design Methods) project, an EU-funded initiative, targets high AR wing design by incorporating wing shape control and load alleviation into a Multidisciplinary Design Optimization (MDO) toolchain, aiming for high efficiency. Within the scope of FLIPASED, this work focuses on wing shape control with trailing edge control surfaces to reduce drag for enhanced aerodynamic efficiency. For an accurate assessment of how wing shape control impacts performance, it is crucial to model drag with high precision. Moreover, the MDO process inherently demands fast simulation capabilities to evaluate numerous design configurations rapidly. To meet these requirements, the following potential-theory based methods are explored:

- a. Vortex Lattice Method (VLM) based near-field implementation.
- b. Doublet Lattice Method (DLM) based far-field implementation.
- c. 3D Panel Method based software Panukl.

In contrast to the VLM/DLM methods which model the lifting surface as a flat panel, the software Panukl models the lifting surface using a 3D panel geometry, which can account for thickness effect. In the paper [4], different potential flow methods has been explored for drag modelling on a UAV configuration. This paper focuses on the D150 model, which represents a market-demanding short-to-medium-range aircraft type. Furthermore, aircraft with two versions of ARs have been investigated to assess the drag reduction impact in both the current aircraft configuration and potential future high AR wings. Different control surface layouts are investigated to determine the optimal layout for drag reduction. A broad range of flight conditions is encompassed in the simulations. By examining different configurations and flight conditions, these studies aim to identify optimal strategies for reducing drag. The findings from these simulations provide valuable insights into potential improvements in aircraft design and operational efficiency.

This paper is organized as follows: Section 2 describes the methods used in the study. Section 3 details the model used in the simulations. Section 4 discusses the studies conducted and the results obtained. Section 5 summarizes the findings, their implications for future aircraft designs and outlines further research directions.

2 DRAG MODELLING AND OPTIMSATION METHODS

This section describes the various induced drag modeling methods utilized in this paper, detailing the theoretical underpinnings and practical applications of each approach. It also ex-

plains how the drag optimization problem was formulated, including the specific objectives, constraints, and variables considered.

2.1 Near field method

The Athena Vortex Lattice (AVL), developed by Mark Drela, is an aerodynamic solver utilizing the Vortex Lattice Method (VLM). This method enables the aerodynamic analysis of rigid aircraft with various configurations [5]. To evaluate induced drag, AVL can compute the induced downwash at the quarter-chord point of each box in the mesh, tilting the local lift vectors and consequently deriving the induced drag, a process often referred to as near-field method.

The near field method discussed in this paper is implemented by coupling AVL with Nastran SOL101 to address aircraft flexibility. Nastran SOL101 is a static analysis routine used to calculate the elastic deformation of an aircraft under specified loads. This coupling process is depicted in the flowchart of Figure 1. Initially, AVL computes the aerodynamic loads, which
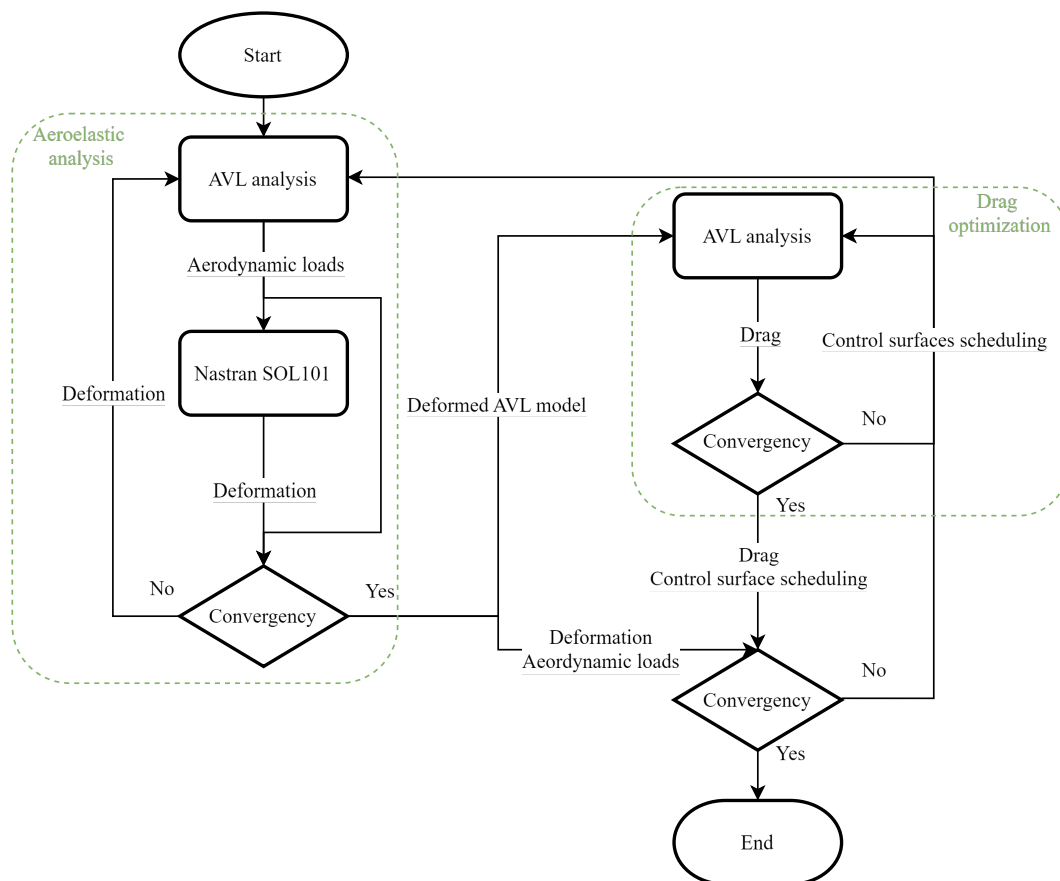

Figure 1: Flowchart for near field implementation

are then applied to the aircraft structure using the rigid body splining method. Subsequently, the structural deformations, calculated using Nastran's static solution, are superimposed onto the original geometry. This deformed geometry is then remeshed. The iterative process continues until convergence is achieved in either the deformations or the aerodynamic loads, marking the completion of the aeroelastic analysis.

Drag optimization is carried out based on the deformed AVL shape in the aeroelastic analysis. The goal is to minimize the objective function $f(\delta)$, which represents the lift-induced drag of the entire configuration, including the trim drag. The optimization is constrained such that the

3

deflections δ of the n control surfaces remain within a specified range. The control surfaces' deflections are the design variables, and their optimal scheduling is sought to achieve minimal inviscid drag. The optimization problem is structured as follows:

$$\begin{aligned} \underset{\delta}{\text{minimize}} \quad & f(\delta) \\ \text{subject to} \quad & \delta_{min} \leq \delta_i \leq \delta_{max}, \quad i = 1, 2, \ldots, n. \end{aligned}$$

The BOBYQA optimization algorithm, available in the NLOPT Python package, is utilized to solve this problem [6].

During the drag optimization phase, the geometry is held constant to expedite the optimization process by excluding the need for flexible AVL analysis at each evaluation of drag. To ensure that the entire process converges to a consistent state in terms of deformation, control surface scheduling, and drag, the flexible AVL analysis and drag optimization are performed iteratively. A final convergence check is conducted to verify that the desired outcomes have been achieved.

2.2 Far field method

In the far field method, the induced velocity is assessed not at the quarter chord point but on the wake surface far downstream from the aircraft, specifically on the so-called Trefftz plane. The induced drag calculations are then performed on this plane. The far field method implemented in this paper is similar with the methodology described in [4, 7].

The implementation relies on MSC Nastran, which is a Doublet Lattice Method-based solver. Utilizing the Kutta-Joukowski theorem (equation 1), the stripwise circulation Γ_i is derived from the stripwise force L_i, as calculated within Nastran. Here, L_i encapsulates the contributions from the individual boxes of each aerodynamic strip, as illustrated in Figure 2.

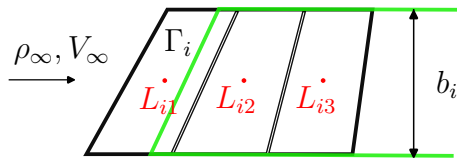$$\Gamma_i = \frac{L_i}{\rho_\infty V_\infty b_i} \tag{1}$$

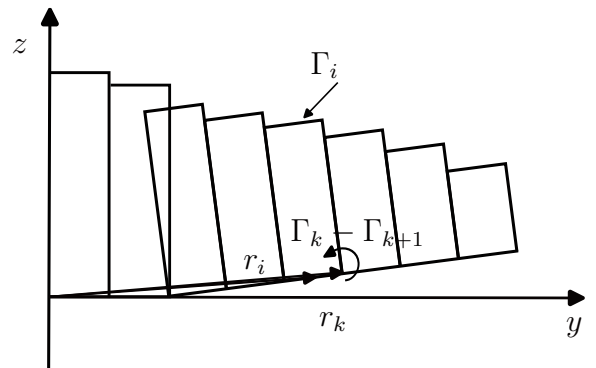Figure 2: Aerodynamic strip mesh in Nastran

Figure 3: Circulation distribution and trailing vortices viewed from Trefftz-plane

Employing the Biot-Savart Law, the downwash—perpendicular to the wake surface—induced by the trailing vortex $\Gamma_k - \Gamma_{k+1}$, is evaluated at the midpoint between stripwise trailing vortex pairs, illustrated in Figure 3. This assessment is conducted using Equation 2.

4

$$w_i = \left(\frac{1}{4\pi}\right) \sum_{k=1}^{N} \left[(\Gamma_k - \Gamma_{k+1}) \left(\frac{1}{|r_i - r_k|} - \frac{1}{|r_i + r_k|} \right) \right] \quad \text{for } i = 1, \ldots, N \qquad (2)$$

Using the small angle assumption, the induced angle of attach at wake strip i is approximated as:

$$\alpha_{i_{induced}} \approx \frac{-w_i}{V_\infty} \qquad (3)$$

The induced drag for each strip D_i is then calculated using:

$$D_i = L_i \alpha_{i_{induced}} \qquad (4)$$

To find the total induced drag across all wake strips, the individual drags are summed:

$$D_{induced} = \sum_{k=1}^{N} D_i \qquad (5)$$

These equations (1-5) are implemented in a Python script to facilitate computational analysis. The optimization problem is formulated same as the method described previously for the near field approach.

2.3 3D panel method

PANUKL is a software package developed in Poland, designed to calculate the aerodynamic properties of an aircraft utilizing the 3D panel method. It creates thick, volumetric surfaces for modeling the aircraft body where the rectangular panel elements represent the flow only and not the actual object. On each surface, one doublet sheet and one source sheet is placed. The vortices on the body are not included in this method, instead rectangular doublet sheets are assumed to be equivalent to a ring vortex. The vortex wake is planar and parallel to the chord, originating from the trailing edge points.

The prime target of the method is to solve the Laplace equation for the full velocity potential, assuming inviscid and irrotational fluid flow [8]:

$$\nabla^2 \Phi_{velo} = 0 \qquad (6)$$

The full velocity potential is defined as the surface integrals of the doublet and source strengths normal to the surfaces:

$$\Phi_{velo}(x, y, z) = \frac{1}{4\pi} \int_{Body+Wake} \mu \frac{\partial}{\partial n} \left(\frac{1}{r} \right) dS - \frac{1}{4\pi} \int_{Body} \sigma \left(\frac{1}{r} \right) dS \qquad (7)$$

The assumption of three boundary conditions follows:

I.) The Dirichlet boundary condition specifies the value of the potential function inside each panel:

$$\frac{1}{4\pi} \int\limits_{Body+Wake} \mu \frac{\partial}{\partial n} \left(\frac{1}{r} \right) dS - \frac{1}{4\pi} \int\limits_{Body} \sigma \left(\frac{1}{r} \right) dS = 0 \qquad (8)$$

where:
- Doublet Strength: $\mu = -(\Phi_{velo} - \Phi_i) = -\varphi$
- Source Strength: $\sigma = \frac{\partial \mu}{\partial n}$

II.) Kutta-Joukowsky condition on the trailing edge id defined as:

$$\Delta p(x, y)_{TE} = 0 \qquad (9)$$

It can be applied to compute the unknown doublet strength on the vortex wake (W) which can be derived from the difference between the doublet strength on the upper (U) and lower (L) side adjacent to the trailing edge (TE):

$$\mu_{TE} = \mu_W = \mu_U - \mu_L = const \qquad (10)$$

III.) On the vortex wake:

$$\frac{\partial \varphi(x, y)}{\partial x} = 0 \qquad (11)$$

The aircraft's body surface is discretized by flat panels, which allows to approximate equation (8) with a set of linear algebraic equations containing unknown doublet strength, that is constant for panel:

$$\sum_{k=1}^{N} C_k \mu_k + \sum_{l=1}^{N_w} C_l \mu_l + \sum_{k=1}^{N} B_k \sigma_k = 0 \qquad (12)$$

where C_k, C_l and B_k denote influence coefficients:

$$C_k = \frac{1}{4\pi} \int\limits_{S_{1234}} \frac{\partial}{\partial n} \left(\frac{1}{r_k} \right) dS_k; \qquad (13)$$

$$C_l = \frac{1}{4\pi} \int\limits_{S_{1234}} \frac{\partial}{\partial n} \left(\frac{1}{r_l} \right) dS_l; \qquad (14)$$

$$B_k = -\frac{1}{4\pi} \int\limits_{S_{1234}} \frac{1}{r_k} dS_k \qquad (15)$$

Meaning of indexes in equations (12)-(15):

N = number of panels on the aircraft surface;
N_w = number of panels on the wake;
S_{1234} = area of the kth panel.

The source strength σ, also constant for each panel, can be defined as the main component of the radial normal velocity on each panel:

$$\sigma = -n \cdot V_\infty \qquad (16)$$

6

This completes the set of equations, only the integrals in formulas (13-15) have to be determined, resulting in the velocity potential distribution on the body surface. At this point, the previously defined full velocity potential (7) can be obtained.

The gradient of the velocity potential results in velocity distribution, which can be achieved by differentiation of Φ_{velo} with respect to defined tangential coordinates. With the application of Bernoulli's theorem, the pressure distribution can be derived. The induced drag can be calculated by using Trefftz plane method in the program. This defines the downwash generated by the aircraft in a rectangular area placed behind the object and derives the induced drag.

In order to achieve true trim flight conditions before deformation calculation a modeling method was derived in which the angle of attack and the elevator deflection were determined such that the lift equals the weight of the aircraft and the value of pitching moment is zero.

3 AIRCRAFT MODEL

The D150 configuration was developed within the DLR project VAMP [9]. It is comparable to the Airbus A320-200 aircraft. Data published by the manufacturer and input data to the preliminary design program PrADO for the application example Airbus A320, are collected for the D150 configuration [10]. Its geometry is shown in Figure 4.
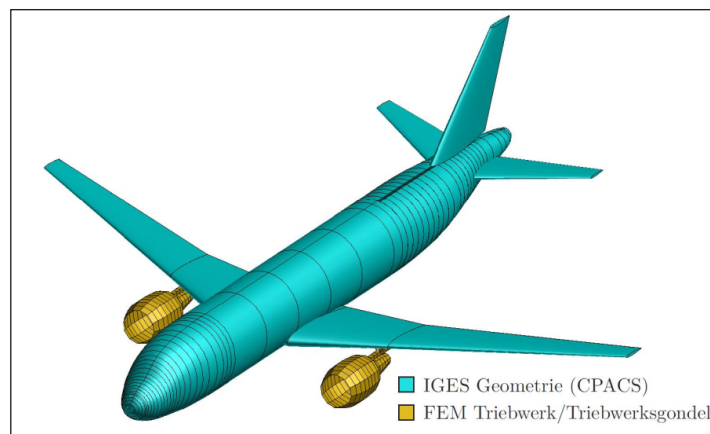
Figure 4: IGES-geometry of the D150-configuration

3.1 Nastran model

The parameterized aeroelastic structural design process CPACS-MONA [11] was used to generate the aeroelastic model. Figure 5 shows the structural model of the D150 configuration, where the fuselage is modeled as a beam. For the wing, horizontal tailplane(HTP), and vertical tailplane(VTP), the load-carrying wing box is modeled, with ribs, spars, and skin represented as shell elements and stringers modeled as beam elements. Both structure mass and fuel mass are clamped to the load reference axis. Figure 6 displays the Nastran aerodynamic model. Given that only symmetrical maneuvers in cruise conditions are considered, the VTP and vertical part of the fuselage do not contribute to lift and are omitted from the aerodynamic model to reduce computational efforts.

3.2 Panukl model

The determination of the aeroelastic trim wing shape requires a structural model to compute the deformation of the aircraft due to the loads acting upon it. A finite element model was created
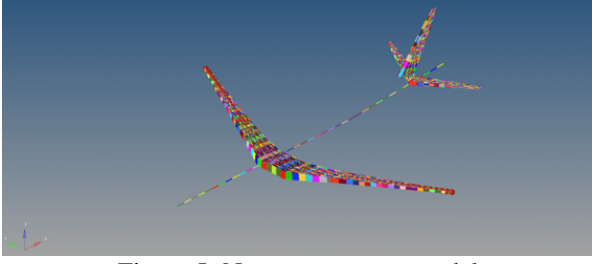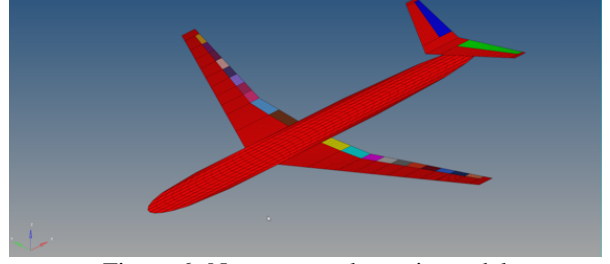
Figure 5: Nastran structure model

Figure 6: Nastran aerodynamic model

in Matlab environment based on the structural properties. Surface spline theory was applied for the interconnection of the aerodynamic and structural models. First an undeformed geometry is generated in Panukl based on the chosen aircraft. The geometry and the computed load on the airframe are extracted from Panukl files to be used in the Matlab code. The code uses this data to calculate and transform the load on the aircraft to the structural model using the surface spline technique. The output from the structural representation is the deformation due to the applied load. This deformation is transformed to the aerodynamic model and a new deformed geometry can be built in Panukl based on this data. The iterative process continues until sufficiently low variation of trim conditions are achieved [12].

The finite element model is constructed by a finite number of beams and nodes, each with unique structural and geometric properties. For the D150 aircraft, the structural model assigns 6 degrees of freedom for every node and the system can be represented in modal coordinates as

$$M\ddot{\eta} + C\dot{\eta} + K\eta = F \tag{17}$$

where modal mass (M), damping (C) and stiffness (K) matrices define how the structure will respond to the external force (F) expressed in modal coordinates (η). A vector u_{node} can be defined for each node that represents the displacements in all the possible directions. With the help of the mode shape matrix Φ_{mode} the displacement vector can be determined for the complete structural grids.

$$u_{struc} = \Phi_{mode}\eta \tag{18}$$

The surface spline theory is a grid interpolation technique to convey data for transformation from aerodynamic grid to structural grid and vice versa, therefore fulfilling an intermediate role. The method calculates unknown deformation at any given location. It uses thin plate deformation that is limited to deform only in the direction perpendicular to its surface. To fulfill the function of a thin plate a spline grid was created to represent the 6 DoF of the structural grid using only heaving motion. The layout is based on both the structural and aerodynamic grid: the structural nodes are connected to each other and all of them are supplemented with two extra nodes in opposite direction. Stiff rods are placed between the nodes. The spline grid structure of the wing can be seen in Figure 7 with color and the black nodes and rods illustrate the structural points.

T_{spline} matrix performs the described transformation from the FEM model to spline grid:

$$u_{spline} = T_{spline}u_{struc} \tag{19}$$

As the second step, to complete the full structural deformation transformation, an interpolation from the spline grid onto the aerodynamic grid is done using T_{plate}. This allows to determine
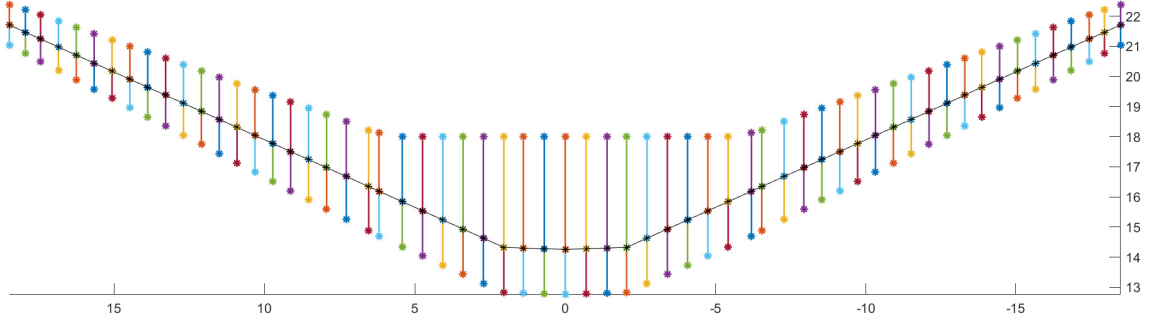
Figure 7: Illustration of structural and spline models

deformation at specific aerodynamic points with the help of the known deformation of the spline grid. T_{as} is the matrix to complete the overall transformation and the deformed aerodynamic mesh can be seen in Figure 8:

$$T_{as} = [T_{spline}][T_{plate}] \tag{20}$$

The transformation of the obtained aerodynamic forces and moments from Panukl happens with reversing the previous two steps. The load components, normal to the thin plate are reduced in the spline nodes in forms of forces only. Following, the forces are converted onto the structural grid points in the form of modal forces, using the mode shape matrix as shown previously.

The determination of optimal control surface scheduling requires aeroelastic results data corresponding to different combinations of flap deflections simulated in Panukl and Matlab. A function can be fitted on the generated data that contains the induced drag, angle of attack, elevator and control surface deflection values. From here, Matlab's fminsearch optimization function was used to derive the optimal scheduling and thus the reduced induced drag value.
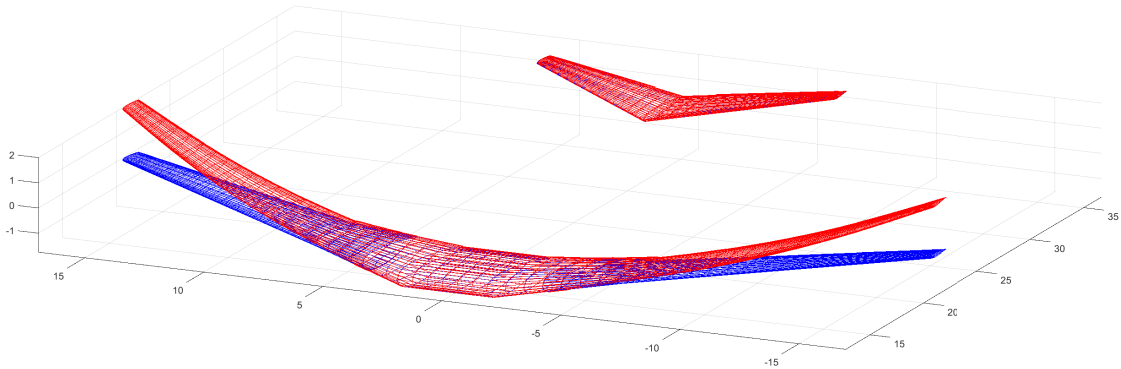
Figure 8: Illustration of of the deformed aerodynamic mesh

4 RESULTS

This section presents the simulation results derived from the aforementioned methods. Additionally, it details the outcomes of the control surface layout study and the AR study conducted to evaluate their influences on drag reduction effect.

9

4.1 Optimal control surface scheduling

To assess the potential for drag reduction, the cruise flight condition was simulated, where the majority of fuel consumption occurs. The design cruise condition assumed for the simulation is Mach 0.78 and altitude 10,000 meters. During the simulation, the aircraft was maintained in a trimmed state, characterized by specific angles of attack(AOA) and elevator deflections.

To fully exploit the potential for drag reduction, there is no limitation on the direction of control surface deflections. Therefore, all control surfaces are treated as multi-functional, capable of deflecting both upwards and downwards. However, to maintain sufficient control authority, the deflection of these control surfaces is restricted to 12 deg, as noted in paper [13]. This configuration optimizes aerodynamic performance, while ensuring the aircraft remains capable of executing necessary maneuvers.

The drag optimization results obtained using the far field method are first presented. Figure 9 illustrates the lift distribution across the wing and fuselage in three scenarios: the reference case, the drag-optimized case, and the elliptical case. An overall elliptical pattern is pursued during the optimisation. Notable deviations between the elliptical and optimal lift distributions
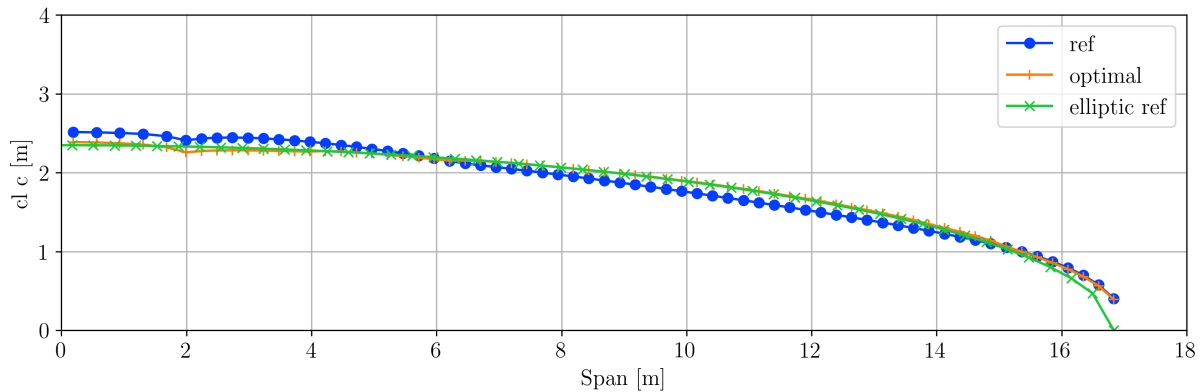
Figure 9: Lift distribution of wing with the far field method

at the wing tips are observed. These deviations are attributed to the absence of control surfaces in these regions, making them solely influenced by the surrounding airflow and the AOA. A similar situation occurs in the fuselage area, where the angle of attack is adjusted to better match the lift distribution, considering its significant impact on drag. Figure 10 depicts the scheduling of control surfaces optimized for minimal drag. The related trim data are detailed in
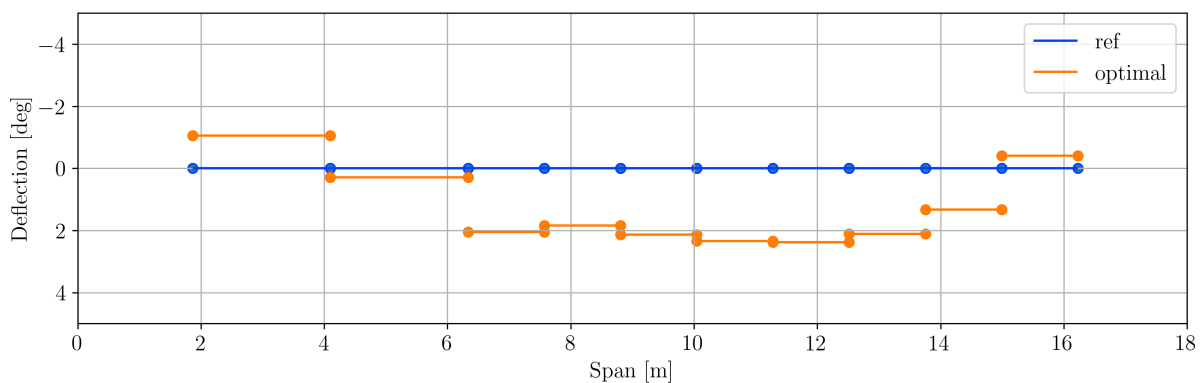

Figure 10: Control surface scheduling with the far field method

Table 1.

Table 1: Trim data.

Case	AOA [deg]	elevator [deg]	C_d	reduction [%]
ref	2.9572	-1.5285	0.00904	-
optimal	2.7367	-2.1651	0.00889	1.64

Figure 11 illustrates the breakdown of lift among the various lifting surfaces, while Figure 12 details the variations in lift across these surfaces. The lift on the wing has increased due to
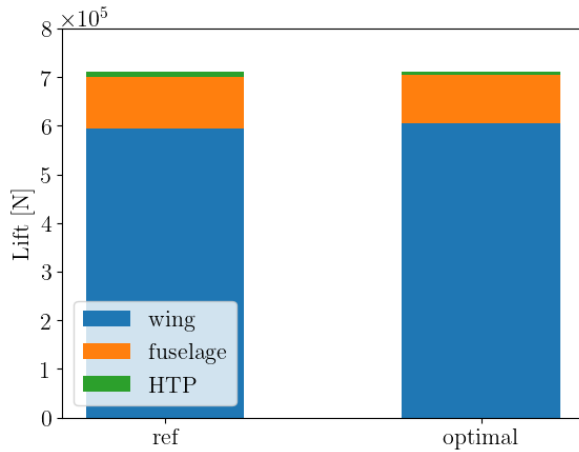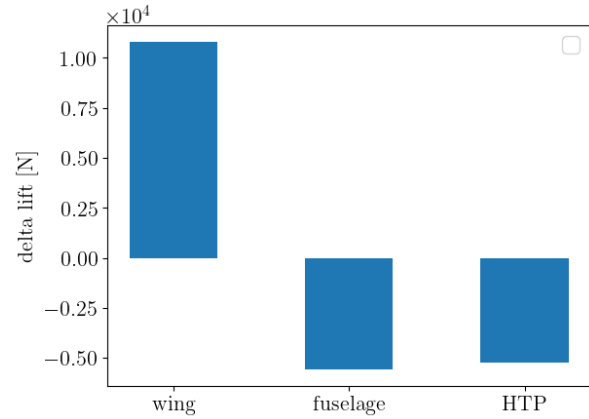

Figure 11: Lift breakdown

Figure 12: Lift variation

the downward deflection of the control surfaces. To maintain the total lift constant, the AOA has been decreased. This increase in lift, primarily in the outer wing areas, provides a greater pitching down moment, thereby reducing the pitching moment required from the horizontal tail plane (HTP). As a result of the decreased AOA and the increased upward deflection of the elevator, there is a corresponding decrease in lift on the HTP.

Figure 13 presents the breakdown of drag across different components of the aircraft, while Figure 14 depicts the variations in drag. By optimizing the lift distribution on the wing and
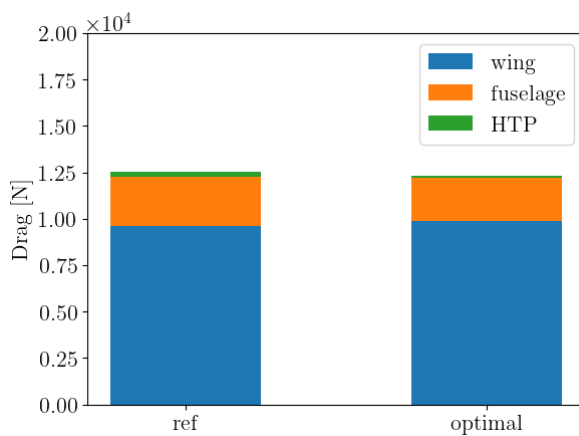
Figure 13: Drag breakdown
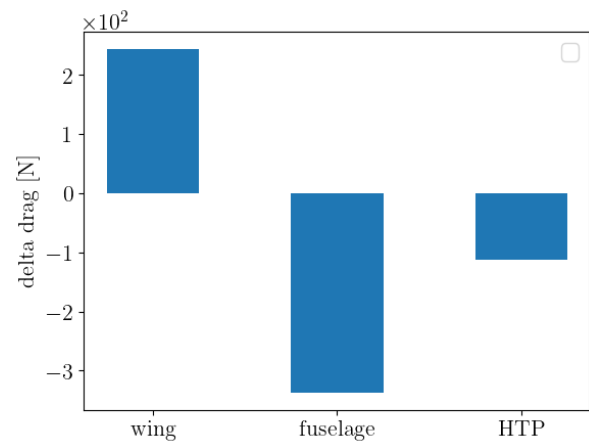
Figure 14: Drag variation

fuselage, the overall drag has been reduced. Additionally, the trim drag originating from the HTP has also decreased due to the reduced lift needed for trimming purposes. Collectively, these adjustments have resulted in an overall drag reduction effect of 1.64%.

A comparison was conducted to analyze the results of drag optimization using both the near field and far field methods. As shown in Figure 15, despite a slight deviation observed in the reference case, an almost identical lift distribution was targeted using either method. This minor
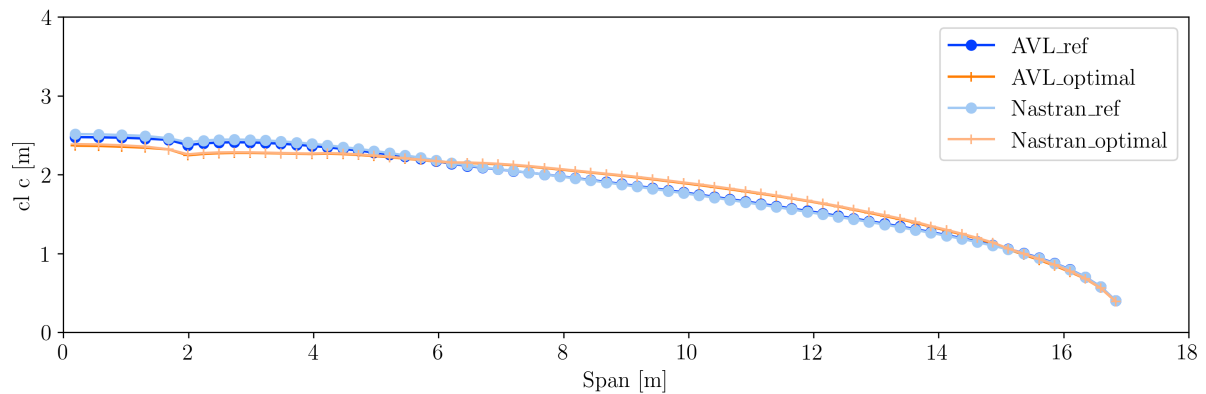

Figure 15: Comparison of lift distribution of wing

deviation could potentially be attributed to the inherent differences in how each method models the flexibility of the aircraft. Figure 16 displays a similar trend in the optimal scheduling of control surfaces between the two analyzed methods. The observed deviation is attributed
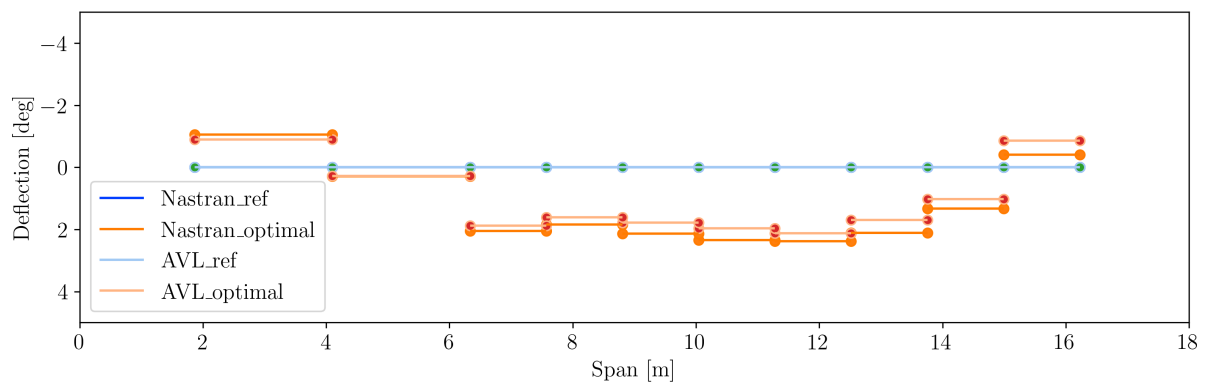
Figure 16: Comparison of control surface scheduling

primarily to two factors: the initial differences in the reference case and the distinct modeling approaches for control surfaces employed in AVL and Nastran. However, the consistency in achieving similar lift distributions and control surface scheduling underscores the effectiveness of both approaches in optimizing the induced drag of the aircraft. For subsequent studies, the results will be exclusively presented using the far field method.

Due to operational constraints, an aircraft might not always operate under designed cruise conditions. Therefore, a broad spectrum of flight conditions has been simulated to provide a realistic overview of the potential drag reduction effects. Figure 17 illustrates the drag polar, which covers a range of flight speeds from Mach 0.75 to 0.82 and altitudes from 7,000 to 11,500 meters. From Figure 18, it is observed that drag reduction effects ranging from 1.5% to 2.5% can be expected, depending on the specific flight conditions. This variability underscores the importance of wing shape control that can adapt to different operational scenarios to optimize performance and efficiency effectively.
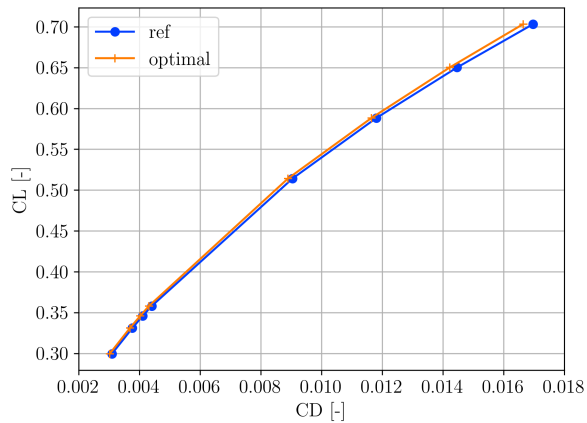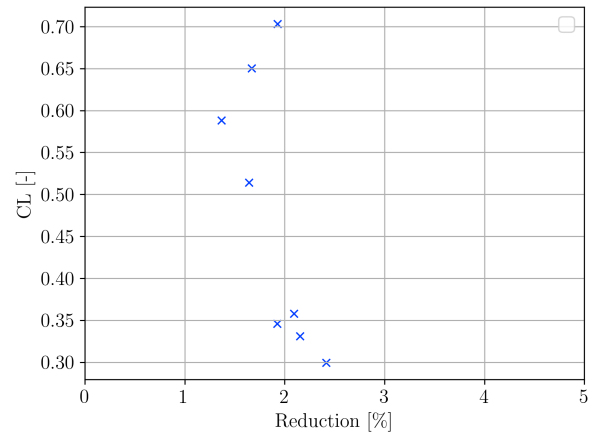
Figure 17: Drag polar

Figure 18: Drag reduction

4.2 Control surface layout study

To determine the most effective control surface layout that requires fewer control surfaces while still achieving significant drag reduction, a comparative study was conducted. This study examined two additional control surface layouts:

- State-of-the-Art A320 Layout: Represented in Figure 19, this layout includes an inner flap, outer flap, and aileron. This traditional configuration serves as a benchmark for comparing newer, potentially more optimized layouts.
- Enhanced Split Flap Layout: Illustrated in Figure 20, this layout modifies the outer flap region by dividing it into three separate control surfaces. This design aims to provide more granular control over the aerodynamic properties of the wing, potentially enhancing the drag reduction capabilities.
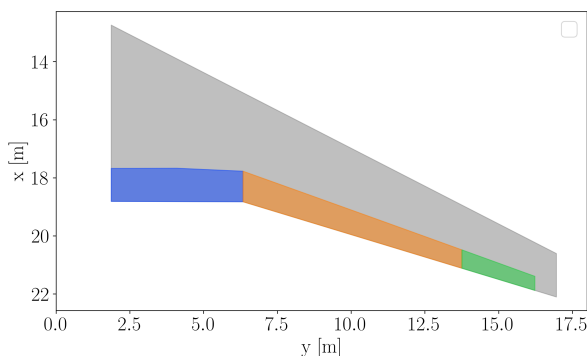
Figure 19: Layout of 3 control surfaces
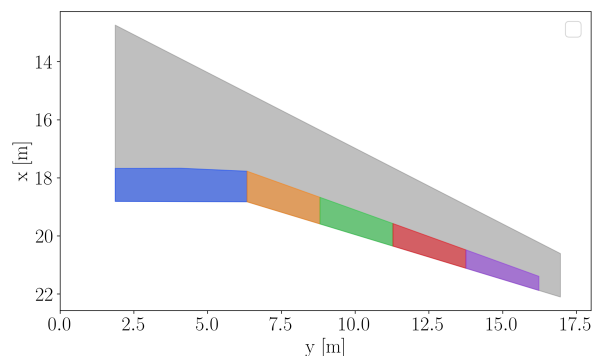
Figure 20: Layout of 5 control surfaces

The previous 10 control surface layout is an evolution of a 5 control surface layout, where each control surface was further split into two.

Considering that multi-functional control surfaces increase system complexity, a further study was conducted to investigate the drag reduction effects while limiting control surface deflections. This study specifically restricted flaps to only downward deflections, adhering to the constraints of current technology levels. By focusing on a simpler, more traditional approach to control surface functionality, the study aimed to evaluate how effective drag reduction can be achieved without the additional complexities introduced by upward deflection capabilities. This approach helps in assessing the potential for drag reduction with a more conservative, technologically feasible control surface design.

13

Figure 21 illustrates the effects of increasing the number of control surfaces on drag reduction at cruise condition. The results indicate that adding more control surfaces yields only a slight
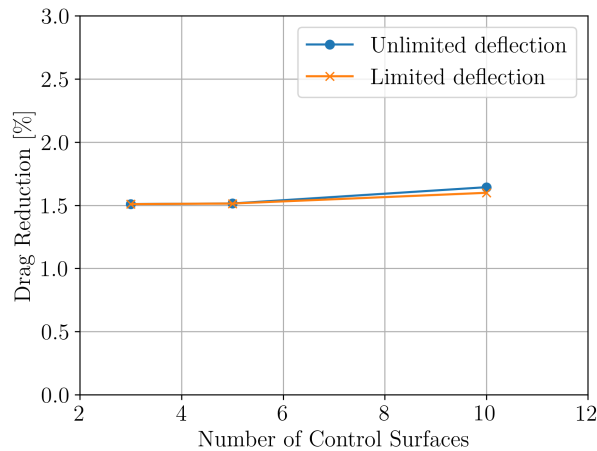

Figure 21: Drag reduction vs number of control surfaces

improvement in performance.

In Figure 22 and Figure 23, it is evident that both the 3 and 5 control surface configurations achieve almost identical lift distributions and control surface scheduling, suggesting that additional surfaces do not significantly enhance drag reduction. The 10 control surface case allows for a more gradual control surface scheduling, which results in marginally better drag reduction effects. However, when deflection is restricted, the impact on drag reduction is negligible for the 3 and 5 control surface cases, as upward deflection is not necessary at simulated flight condition, as shown in Figure 23. For the 10 control surfaces layout, limiting control surface deflection decreases the effectiveness of drag reduction.
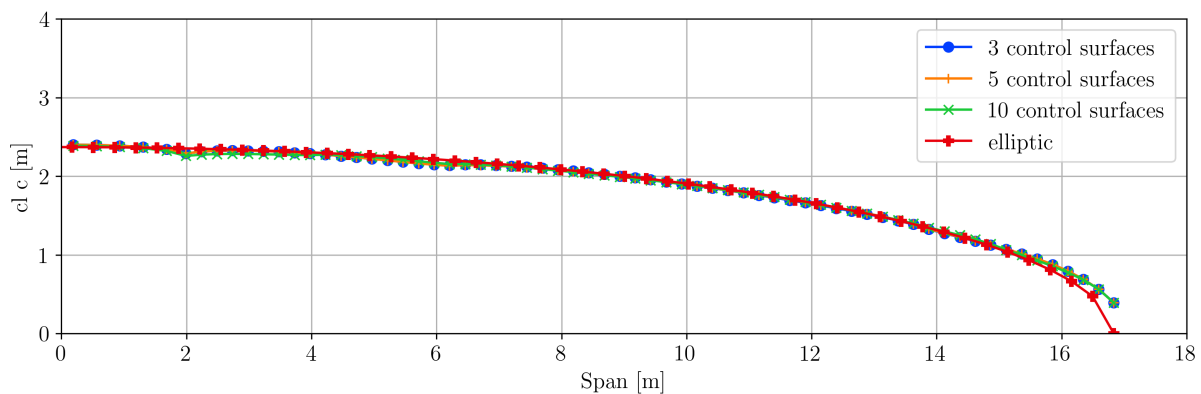

Figure 22: Comparison of lift distribution on the wing among different layouts of control surfaces

The same range of flight conditions was simulated for three control surfaces layout, but with limited deflection. As illustrated in Figure 24, the layout featuring ten control surfaces without deflection limitations consistently delivers better drag reduction performance. The advantage of having more control surfaces becomes particularly apparent in high dynamic pressure cases. In such scenarios, the ability to adjust the inner flaps upwards is crucial for fine-tuning the lift distribution to achieve optimal aerodynamic performance. This upward deflection capability allows for more precise control over the aircraft's aerodynamics, enhancing its efficiency under varying flight conditions.
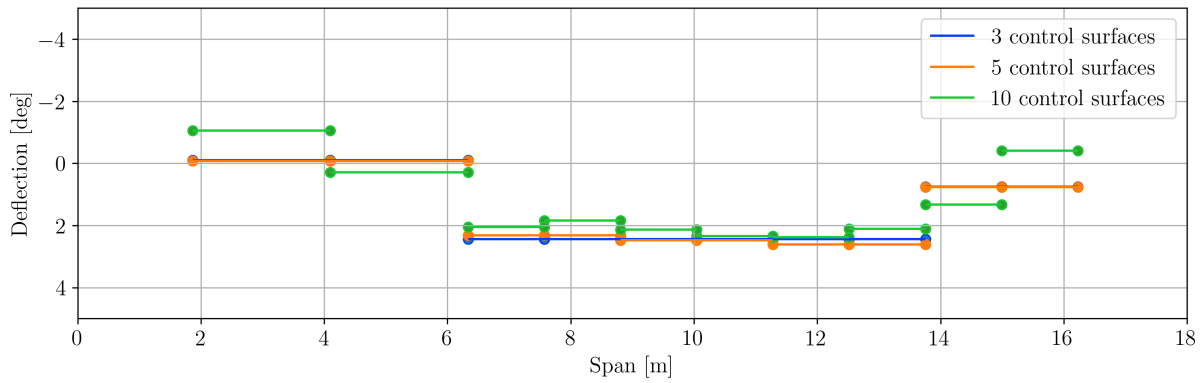
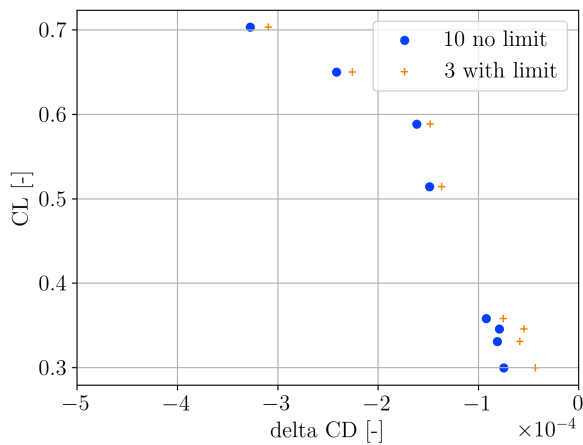Figure 23: Comparison of control surface scheduling among different layouts of control surfaces

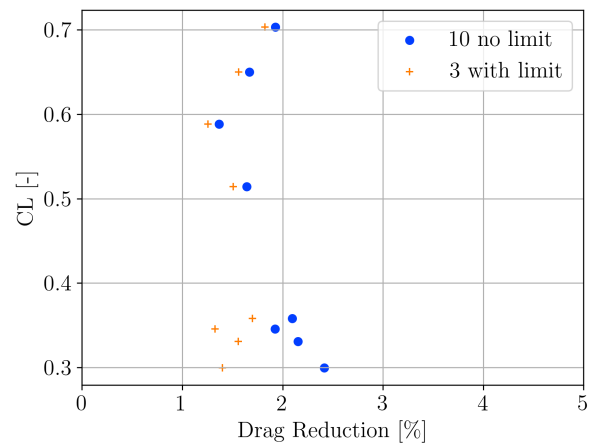Figure 24: Comparison of drag reduction in drag counts

Figure 25: Comparison of drag reduction

4.3 Aspect ratio study

A high AR wing of 11.2 was simulated to investigate its impact on drag reduction effects. Figures 26 and 27 display the optimized lift distribution and control surface scheduling for this AR configuration. The results demonstrate a similar trend to that observed with the AR 9.7
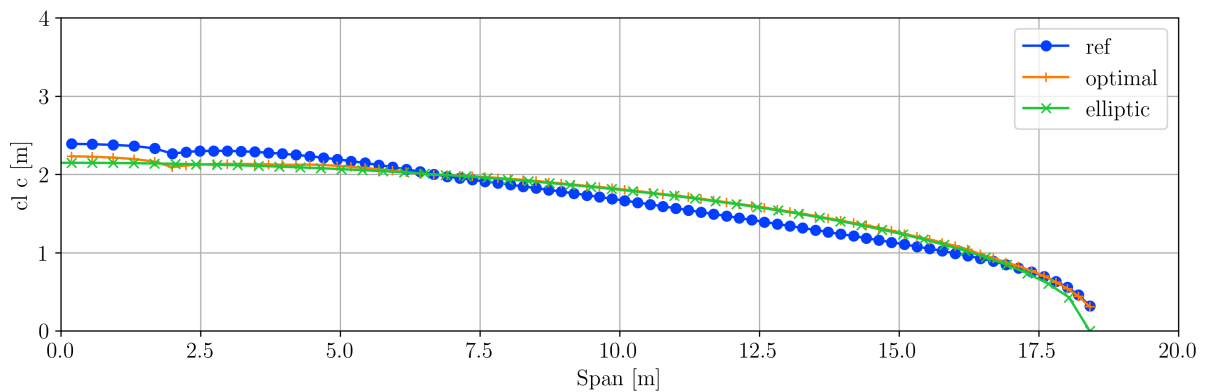

Figure 26: Lift distribution of high AR wing

wing. However, the simulations indicate that a higher drag reduction of 2.8% can be achieved with the AR 11.2 wing, as detailed in Table 2). This improvement in drag reduction with higher AR wings can be attributed to increased wing flexibility, which shifts the lift more inboard. This shift moves further away from the optimal elliptical lift distribution, providing greater potential for wing shape control.
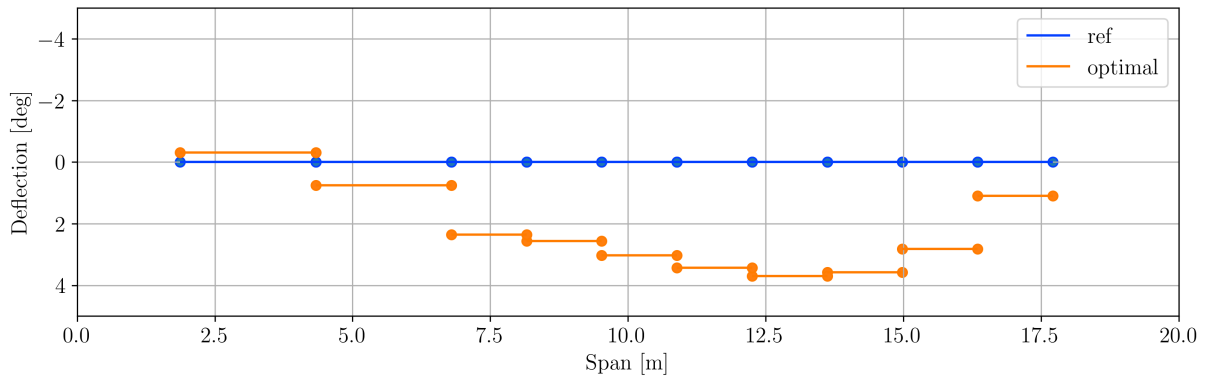
Figure 27: Control surface scheduling of high AR wing

Table 2: Trim data of high AR wing.

Case	AOA [deg]	elevator [deg]	C_d	reduction [%]
ref	2.8663	-1.8182	0.00770	-
optimal	2.4426	-2.4763	0.00748	2.80

Figure 28 demonstrates that for the high AR wing in cruise conditions, increasing the number of control surfaces enhances the drag reduction effects. This is due to the ability to more finely tune the lift distribution. As depicted in Figure 27, only minor upward deflections are needed in the 10 control surface layout. For other layouts, no upward deflection is needed at all. Consequently, restricting the deflection does not impact the overall effectiveness of drag reduction for these configurations.
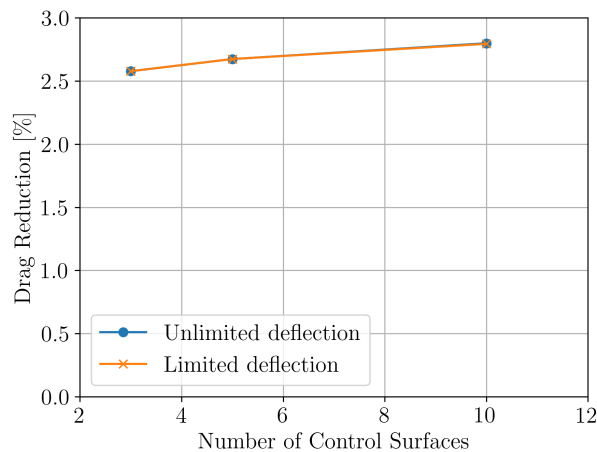

Figure 28: Drag reduction vs number of control surfaces on high AR wing

The same range of flight conditions was simulated for the high AR wing, demonstrating notable drag reduction outcomes. Figures 29 and 30 illustrate that a 10 control surface layout can yield drag reduction effects ranging from 2.5% to 4%. Additionally, with limited deflections in a 3 control surface layout, drag reduction effects of 2% to 3% can be achieved. Consistent with previous observations, the most significant loss in drag reduction effectiveness due to limited deflection occurs in cases of high dynamic pressure.
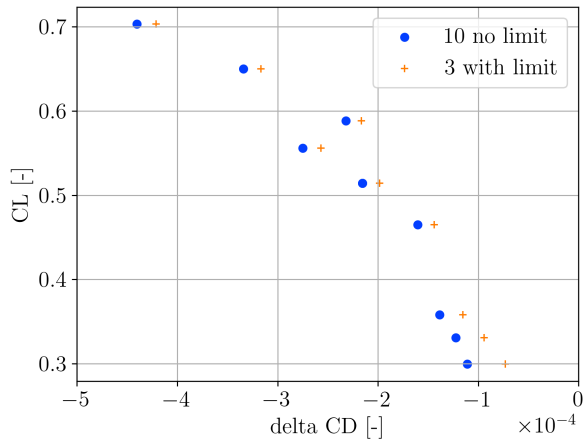
Figure 29: Comparison of drag reduction in drag counts on high AR wing
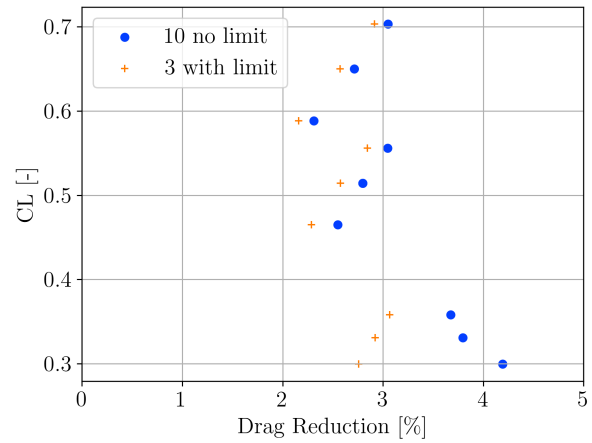
Figure 30: Comparison of drag reduction on high AR wing

4.4 Panukl based study

A 3D panel method based investigation in Panukl was conducted to compare the potential in drag reduction for 5 control surface layout models with AR 9.7 and 11.2 by finding optimal control surface scheduling for each. The cruise flight conditions during the simulations were identical to the ones in previous results, although the fuselage was not included due to its large increase impact on computational demand. The number of iterations between the aerodynamic and structural calculations were set to five thus the convergence of the trim values could be met in all cases.

A series of control surface scheduling combinations were simulated ranging from -1 to 2 degrees from which 320 simulations were used for model fitting. Figures 31-32 illustrate the optimized control surface schedules for the models.
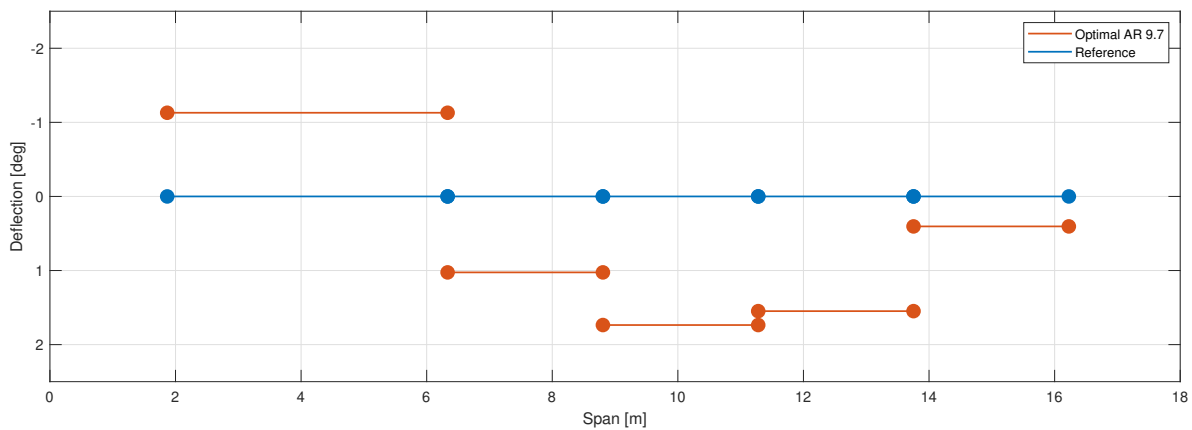

Figure 31: Optimal control surface scheduling of AR 9.7 model based on Panukl

The results for drag reduction are shown in Table 3 where the calculated values refer to the model fitting results and the simulated values were derived from an additional simulation in Panukl with the optimal control surface configuration.

As expected, the higher AR wing allowed a greater induced drag reduction due to its increased
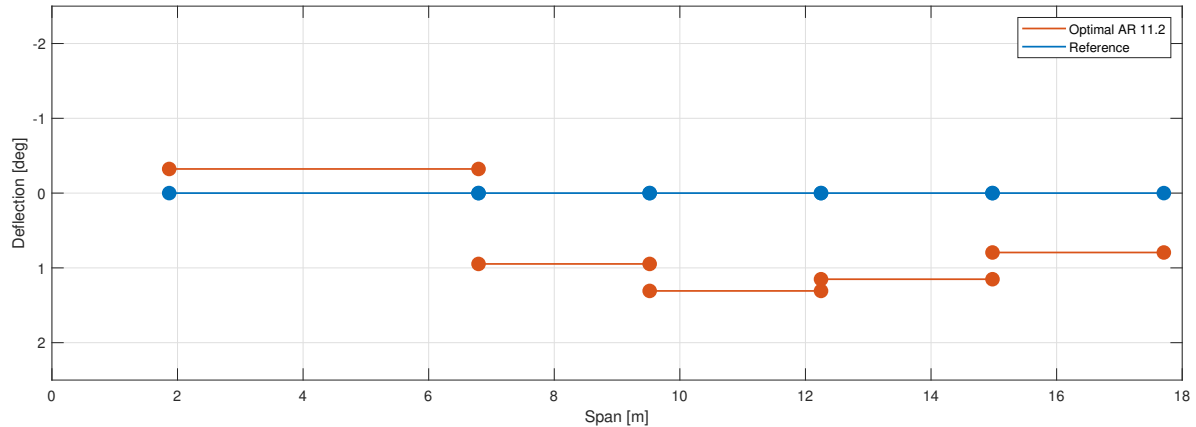
17

Figure 32: Optimal control surface scheduling of AR 11.2 model based on Panukl

Table 3: Comparison of induced drag data for AR 9.7 and 11.2 models in Panukl

Case	C_d	
	AR 9.7	AR 11.2
reference	0.010179	0.008426
calculated	0.009963	0.008014
simulated	0.009909	0.008061
reduction [%]	2.65	4.33

felxibility compared to the nominal case.

5 DISCUSSION AND OUTLOOK

This paper has demonstrated that by employing wing shape control with 10 multifunctional control surfaces, drag reduction ranging from 1.5% to 2.5% can be achieved, depending on flight conditions. The study highlights the effectiveness of the different drag modeling methods and optimization strategies utilized.

While increasing the number of control surfaces generally enhances drag reduction, this benefit must be weighed against the potential weight penalty from additional actuators and auxiliary systems, which could negatively impact aircraft performance. Even with current state-of-the-art control surface configurations, drag reduction effects ranging from 1% to 2% can be achieved. Future work could explore the trade-off between achieving greater drag reduction and managing increased weight.

For wings with higher AR, the drag reduction effects are more pronounced due to increased flexibility from higher ARs. It is important to note that the high AR wing in this study was merely an stretching of the nominal AR model and was not specifically redesigned for optimal performance. A properly redesigned high AR wing could potentially be more efficient, leaving less margin for drag reduction.

The conclusions drawn are based on the specific mass case investigated. Results may vary with different mass cases due to the aeroelastic effects influenced by different fuel loads. Further investigations into additional mass cases are planned for future studies.

Lastly, wing shape control represents a vital strategy for immediate enhancements to current aircraft configurations, requiring no significant structural or aerodynamic design changes. This

approach is especially critical given the urgent need to address the aviation sector's climate impact and reduce CO2 emissions effectively.

6 ACKNOWLEDGEMENTS

7 REFERENCES

[1] Reist, T. A., Koo, D., and Zingg, D. W. (2022). Aircraft cruise drag reduction through variable camber using existing control surfaces. *Journal of Aircraft*, 59, 1406–1415. ISSN 15333868. doi:10.2514/1.C036754. - business jet- three contro surfaces- CFD, no aeroelasticity- 2 mach 3 Cl simulated cases- wing twist and control surface deflection- constraints AOA, airfoil thickness.

[2] Lebofsky, S., Ting, E., and Nguyen, N. (2014). Aeroelastic modeling and drag optimization of aircraft wing with variable camber continuous trailing edge flap. American Institute of Aeronautics and Astronautics Inc. ISBN 9781624102882. doi:10.2514/6.2014-2443. - Generic Transport Model- aero solver Vorlax- surrogate is used.

[3] Nguyen, N. and Xiong, J. (2021). Real-time drag optimization of aspect ratio 13.5 common research model with distributed flap system. doi:10.2514/6.2021-0069.

[4] Meddaikar, Y. M., Kier, T. M., Bartasevicius, J., et al. (2023). Aeroservoelastic induced drag modelling and minimization for the t-flex demonstrator. American Institute of Aeronautics and Astronautics (AIAA). doi:10.2514/6.2023-0176.

[5] Yu, F., Bartasevicius, J., and Hornung, M. (2022). Comparing potential flow solvers for aerodynamic characteristics estimation of the t-flex uav.

[6] Johnson, S. G. (2007). The NLopt nonlinear-optimization package. `https://github.com/stevengj/nlopt`.

[7] Kolonay, R. M. and Eastep, F. E. (2006). Optimal scheduling of control surfaces on flexible wings to reduce induced drag. *Journal of Aircraft*, 43, 1655–1661. ISSN 15333868. doi:10.2514/1.14604.

[8] Goetzendorf-Grabowski, T. and Mieloszyk, J. (2017). Common computational model for coupling panel method with finite element method. *Aircraft Engineering and Aerospace Technology*, 89(5), 654–662. doi:10.1108/aeat-01-2017-0044.

[9] Zill, T., Ciampa, P. D., and Nagel, B. (2012). Multidisciplinary design optimization in a collaborative distributed aircraft design system. In *50th AIAA Aerospace Sciences Meeting including the New Horizons Forum and Aerospace Exposition*. p. 553.

[10] Klimmek, T. (2016). *Statische aeroelastische Anforderungen beim multidisziplinären Strukturentwurf von Transportflugzeugflügeln*. Ph.D. thesis, DLR - Institut für Aeroelastik.

[11] Klimmek, T., Schulze, M., Abu-Zurayk, M., et al. (2019). cpacs-MONA – An independent and in high fidelity based MDO tasks integrated process for the structural and aeroelastic

design for aircraft configurations. In *International Forum on Aeroelasticity and Structural Dynamics 2019, IFASD 2019*.

[12] Olgyay, Á., Takarics, B., Körösparti, B., et al. (2022). Aeroservoelasticity Investigation with Panel Method.

[13] Urnes, J., Nguyen, N., Ippolito, C., et al. (2013). A mission-adaptive variable camber flap control system to optimize high lift and cruise lift-to-drag ratios of future n+3 transport aircraft. ISBN 9781624101816. doi:10.2514/6.2013-214. - aero solver: Vorview- remeshing for different flap settings- with deflection geometry will be deformed and remeshed- in this work no aeroelasticity.

COPYRIGHT STATEMENT